Ex-situ Micro X-ray Computed Tomography Tests and Image-based Simulation of UHPFRC Beams under Bending

Xin Zhang[a], Zhenjun Yang[b,*], Miao Pang[a], Yong Yao[a], Q.M. Li[c] , T. James Marrow[d]

[a] *College of Civil Engineering and Architecture, Zhejiang University, 310058, China.*

[b] *Hubei Key Laboratory of Geotechnical and Structural Safety, School of Civil Engineering, Wuhan University, 430072, China*

[c] *Department of Mechanical, Aerospace and Civil Engineering, The University of Manchester, M13 9PL, UK*

[d] *Department of Materials, Oxford University, OX1 3PH, UK*

Abstract:

Micro-structures of fibre reinforced composites play a pivotal role in their damage, fracture and failure mechanisms. This study first carried out ex-situ micro X-ray Computed Tomography (μXCT) tests of three small ultra-high-performance fibre reinforced concrete (UHPFRC) beams under progressive three-point bending. The first two beams were continuously loaded until failure and their central regions with the main flexural crack were scanned by μXCT before and after the test. The third beam was subjected to five cycles of loading-unloading until failure, and was scanned by μXCT after each unloading. The 3D μXCT images with 30 μm voxel resolution were then processed and analysed, and the spatial distribution, number, orientation and dimension of pores and fibres were statistically quantified. The micro-scale failure mechanisms, such as fibre bridging of cracks, fibre-matrix interfacial slipping and debonding, and matrix failure, were visualised and analysed. The μXCT images of the first two beams were then segmented and directly converted to meso-scale finite element models based on orientation-dependent bond-slip relations for the fibre-matrix interfaces and continuum damage plasticity for the matrix. The simulated load-displacement curves, fracture processes and final crack morphologies were found in excellent agreement with the tests. It was also found that the position, dimension and orientation of fibres and pores have significant effects on the damage and fracture initiation and evolution from both the tests and the simulations.

Keywords: fibre reinforced concrete; X-ray Computed Tomography; Image-based finite element modelling; mesoscale model; damage and fracture; pores.

1. Introduction

Plain concrete's low tensile strength makes concrete structures susceptible to fracture and brittle failure, and therefore, steel fibres are often added to reinforce the concrete due to its wide availability, recyclability and reinforcement efficiency. In the last three decades, a new steel fibre reinforced cemetitious composite material, called ultra-high performance fibre reinforced concrete (UHPFRC), has attracted worldwide attention [1-5]. The mortar matrix is made from cement, fine sands of 0.1-0.6 mm size, micro-silica or silica fume, super-plasticiser, and water with very low water cement ratio (typically ≤ 0.25) [6]. It does not have coarse aggregates. As such, UHPFRC has much higher compressive strength (typically above 120 MPa), much denser microstructures and much higher resistance against chloride erosion, water penetration, freeze-thaw cycles etc., and thus, much better durability than traditional concrete [7]. The fibres used in UHPFRC are 1-10% in volume fraction, 0.15 - 0.2 mm in diameter and are higher than 2000 MPa in strength. The fibres' crack restriction and bridging effects lead to 6-15 MPa tensile strength and up to 40,000 J/mm^2 fracture energy in UHPFRC, making the material ideal for structural protection against impact and blast [8-10]. However, the material cost of UHPFRC is still 3-10 times that of normal concrete, about half of which is from the high-strength steel fibres. This limits its use so far to some niche structural applications. Therefore, material optimisation, especially the amount, spatial distribution, orientation, and geometry of fibres, is essential before the material can be widely applied in engineering practices. This is only possible after the material's microstructure and cross-scale mechanical properties and behaviour including damage and fracture are fully understood.

Recently, micro X-ray computed tomography (μXCT), a 3D imaging technique routinely used in medical scanning, has become popular in characterising the internal nano-, micro- and meso-scale structures of many composite materials, because of its high resolution, non-destructive nature, and clear visualisation of shapes, sizes and distribution of multi-phases including pores and cracks. This technique also allows complicated damage and fracture mechanisms to be studied by scanning the specimen at different times as it is loaded to failure. This in-situ (simultaneous scanning and loading) or ex-situ (scanning after loading-unloading cycles) approach, sometimes called 4D imaging [11], makes accurate investigation of failure modes at small length scales possible. Although μXCT has been used to visualise internal micro-structures and analyze fracture mechanisms of a wide range of materials, such as metal composite material [12], carbon fibre reinforced polymers [13], ceramic matrix composite [14], plain concrete [15], foamed concrete [16], and fibre reinforced concrete (FRC) [17-23], 4D μXCT studies of composites are still very limited, due to the lack of in-situ μXCT facilities and high costs of performing such tests. Our recent study [24] appears to be the only reported 4D μXCT tests of UHPFRC materials, which has demonstrated the powerful capability of this method in visualising and analysing the complicated deformation and failure process of UHPFRC, especially the effects of fibre crack-bridging and orientation.

Apart from revealing internal microstructures and eluciding complicated failure mechanisms with unrivalled resolution, μXCT images can be used to build micro/meso-scale finite element (FE) models for further linear and nonliear analyses under a varieties of environmental factors or loading conditions. Being

able to faithfully descibe the material's micro/meso-structures, including the shape, size and spatial distribution of all material phases. Such models are more realistic and accurate than those with assumed micro/meso-structures. They can also be directly validated against in-situ or ex-situ μXCT tests, both qualitatively and quantitatively, in terms of load-carrying capacities and the whole damage and fracture processes until failure. To date, very limited studies in μXCT image based simulations have been reported, mostly for calculating homogenised elastic properties (e.g., metal composites [12], carbon fibre composites [13], concrete [15], polymer foams [25], and UHPFRC [23]), and rarely for simulating nonlinear damage and fracture and understanding the failure mechanisms (e.g., ceramic composites [14], foamed concrete [16], and plain concrete under quasi-static loading [26, 27] and high-speed impact [28, 29]). No μXCT image based FE simulations of complicated damage, fracture and failure mechanisms have been reported for steel fibre reinforced cementitious composites such as SFRC or UHPFRC.

This study aims to investigate the complicated damage and fracture behaviour and various failure mechanisms of UHPFRC beams under bending, with a particular attention to the effects of steel fibres and pores on crack initiation and evolution, by a combination of ex-situ μXCT tests and meso-scale image-based FE simulations. Three UHPFRC beams are tested under progressive three-point bending. The first two beams are continuously loaded to failure with the cracked central areas scanned by μXCT before and after the test (i.e., post-mortem). The third beam is first scanned by μXCT and then subjected to five cycles of loading-unloading until failure with a μXCT scanning after each unloading. The 3D images are then processed and statistically analysed to characterise microstructural features such as the distribution, number, orientation and dimension of pores and fibres as well as key micro-scale failure mechanisms, such as fibre crack-bridging, fibre-matrix bond-slip, matrix failure for the third beam. After phasic segmentation, the μXCT images of the first two beams are converted to meso-scale FE models. Orientation-dependent bond-slip relations extracted from single fibre pullout tests are used to indirectly model the fibre-matrix interfaces for simplicity of FE mesh generation. The continuum damage plasticity constitutive law is used for the mortar matrix. The simulations are compared with the ex-situ μXCT tests in terms of load-displacement curves, fracture processes and final crack morphologies, with particular interests on the effects of fibre and pores on the damage and fracture evolution.

2. Experimental Study

2.1 Materials

The mixture design of the UHPFRC material is listed in Table.1. The silica fume has a specific surface area of 18,200 m^2/kg and over 95% silica content. Medium sand with a fineness modulus of 2.5 is used. The poly-carboxylic acid superplasticiser is used as the water reducing agent, and the water-binder ratio is 0.2. Copper coated steel fibres with 0.2 mm in diameter, 14 mm in length, 2,400 MPa in strength, and 210 GPa in elastic modulus are added with a designed fibre content of 1% in volume. The UHPFRC material is cured with a temperature of 20±2°C and a relative humidity of 95% for 28 days. Six 70.7mm cubic specimens, three without fibres (i.e., UHPC mortar) and three with 1% fibres (UHPFRC), are tested in compression. The

28-day compressive strength is f_c' =109.51±6.21MPa for UHPC and 120.31±2.05MPa for UHPFRC, respectively. The tensile strength f_t is not tested but estimated as 7 MPa for the UHPC mortar and 11 MPa for the UHPFRC, respectively, according to [30].

Table 1: Mixture proportions of UHPFRC (kg/m^3)

Cement	Sand	Silica fume	Water	Superplasticiser	Steel fibre
822	1150	205	205	6	78

2.2 Test Setup and Results

40 x 40 x 160 mm small beams after 28 days' curing are loaded under three-point bending by an Instron electro-hydraulic servo machine. Fig.1 shows the test setup. A beam is placed on two stainless steel rods and is loaded by another rod at the top center. The distance between the two supports is L=120 mm. Loading is applied by the displacement control at a rate of 0.2 mm/min. Three beams are tested. The first two are loaded continuously until failure, and the third is subjected to five load-unloading cycles. The beams after the test are shown in Fig.2. All the three beams fail with a dominant flexural crack in the middle region, and no minor cracks are visually identified. The cracks are inclined in all the beams.

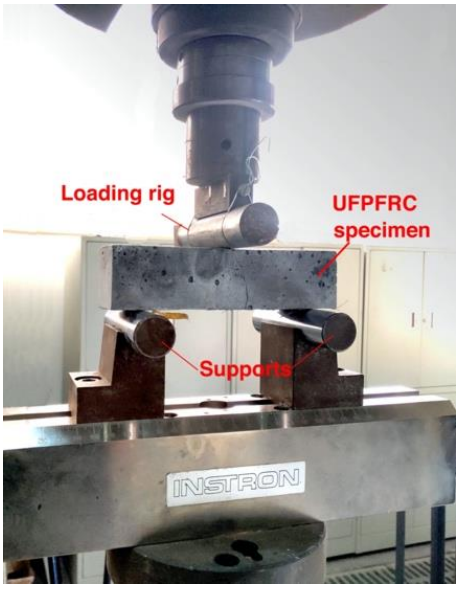

Figure 1 The test setup

(a) Beam 1

(b) Beam 2

(c) Beam 3

Figure 2 Beams after the test

Fig.3 shows the applied load-crosshead displacement curves. For all the beams, the first peak load of 5kN is reached after a short elastic stage and the crack initiation. The flexural strength at the first peak load is calculated as $3P_{max}L/(2bh^2)$ = 14.1 MPa. This is followed by a sharp strength drop (to about 3.4 kN), a short hardening stage to a second peak load representing the maximum bridging strength, and finally a long softening stage indicating the high ductility of UHPFRC. For Beam 1 and Beam 2, the second peak load is lower than the first peak, while for Beam 3, a higher second peak 6.3 kN (with flexural strength 17.6 MPa) than the first is reached during loading in the second cycle. A potential reason for this is the strain hardening

of steel fibres during cyclic loadings but a thorough investigation is needed, which is beyond the scope of this study.

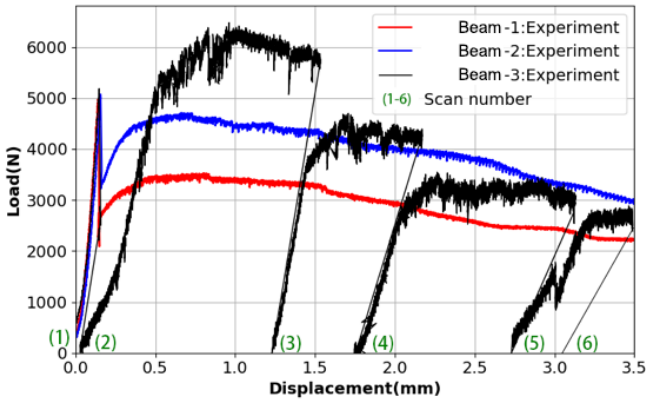

Figure 3 Experimental load-displacement curves for the three beams (The scan numbers for Beam-3 are displayed at unloaded points).

2.3 Ex-situ μXCT tests

μXCT scanning is carried out on a Nikon XTH320LC X-ray Computed Tomography scanner with 180 kV and 160 μA intensity at Zhejiang University, China, as shown in Fig.4. The first two beams are scanned both before and after the test. The third beam is scanned after each unloading, so it is scanned six times in total, as indicated in Fig. 3. To obtain high resolution images, only the central region of about 40 x 40 x 53 mm is scanned for each beam. For each scan, the stage is rotated by 360° with an angular speed of ~0.244°/s, resulting in 2501 2D radiographs with an angular displacement of 0.143° and a pixel resolution of 30 μm.

(a) XCT scanner (b) XCT scanner (inner)

Figure 4 The μXCT facility at Zhejiang University, China

3. μXCT Image Processing, Segmentation and Statistical Analyses

The obtained 2D CT radiographs are first reconstructed into 3D absorption contrast images using CT Pro to obtain a cuboid volume with pixel dimensions of 1200 x 1200 x 1600 along the x, y, and z directions, respectively. The software Avizo is then used to crop and filter these images, segment material phases and visualise fracture patterns. The detailed procedure is shown in Fig.5.

Fig. 6a shows an image slice with noises and original dimensions. The median filter and the non-local means filter are applied to reduce the noise. The former is uses morphological operators to set the grey value of an image pixel (voxel) to the median grey value of its neighborhood pixels (voxels), while the latter further denoises the image using a non-local means approximation based on adaptive manifold which is explained in detail in [31, 32]. The uneven edges are then cropped with negligible reduction to the image volume. The resultant image slice with higher contrast is shown in Fig. 6b. Fig.7 shows the position of the scanned region in the beam with three typical grey-scale images in three normal planes with fibres, pores and cracks labelled after the test. The detailed 3D μXCT images before the test for Beam 1 and Beam 2 are shown in Fig. 8a and Fig. 8b, respectively, where the fibres are in red, the pores are in green and the mortar is rendered transparent. These images will be segemented and converted to meso-scale FE models for simulation.

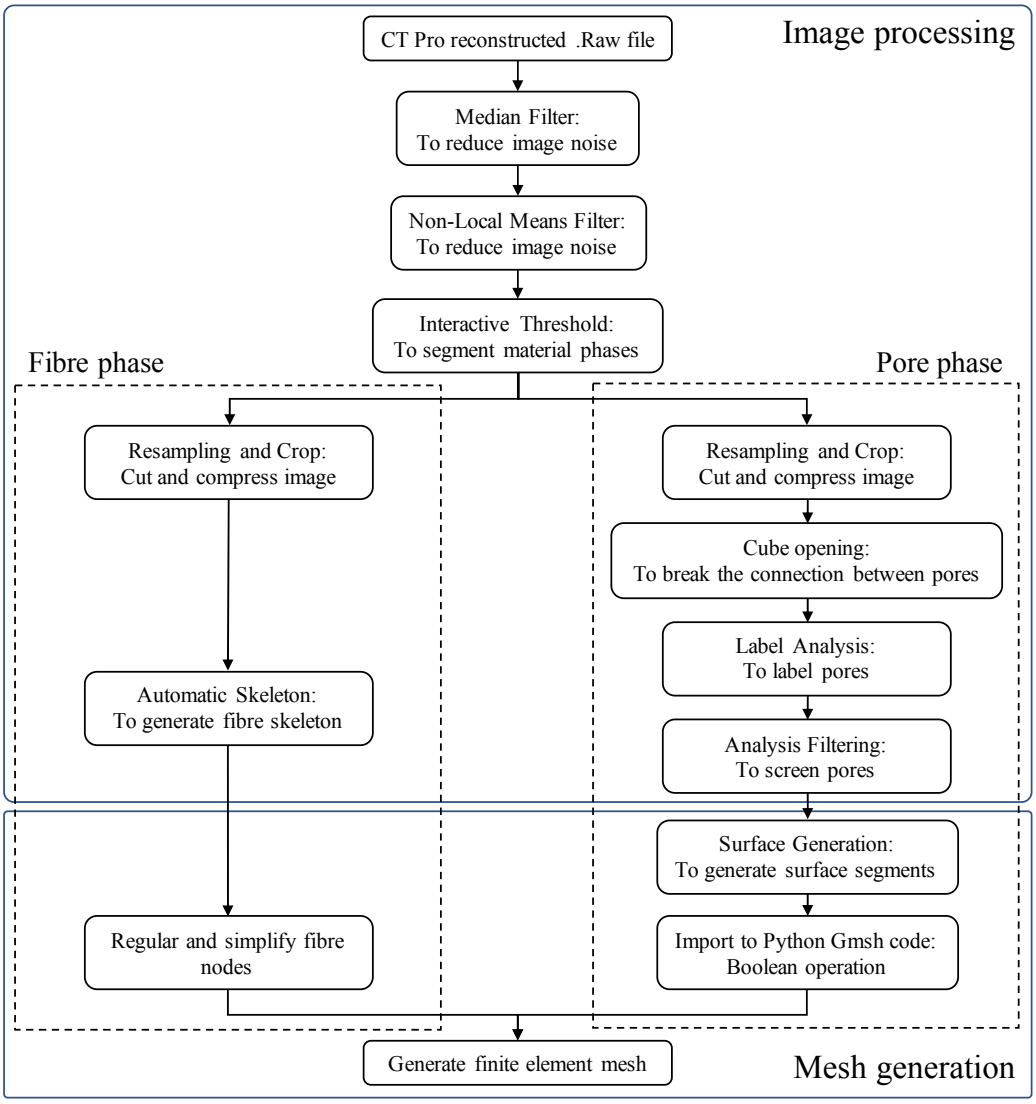

Figure 5 Image processing and mesh generation flow

147

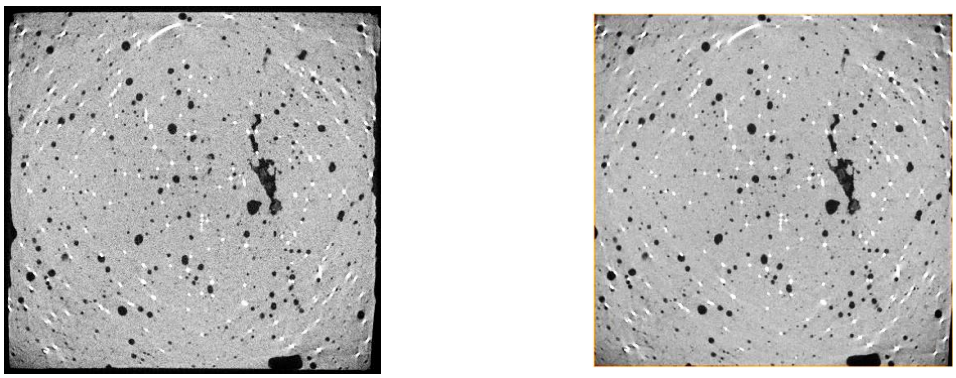

(a) Original (40 x 40 mm) (b) Filtered and cropped (38.9 x 39.1 mm)

Figure 6 a μXCT image slice before and after noise filtering and cropping

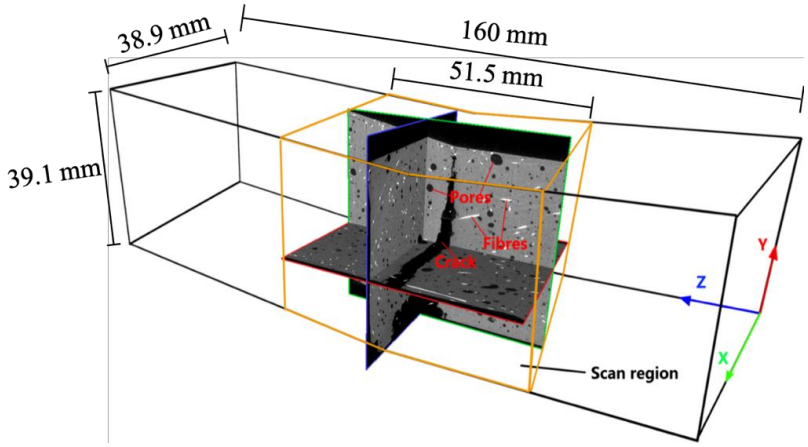

Figure 7 Reconstructed image slices in three normal planes for Beam 1 after the test

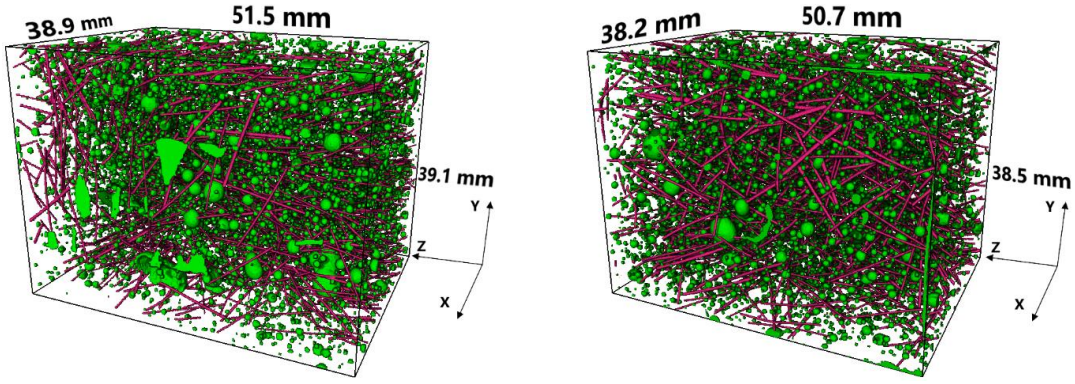

Figure 8 The reconstructed and cropped μXCT volumes before loading for Beam 1 (left) and Beam 2 (right): fibres in red, pore in green and mortar transparent.

148 Material phases in the μXCT images are then segmented according to grey value thresholds. The Line-

149 Probe command is used first, as shown in Fig.9 for Beam 2 as an example. The full grey scale of the image is

0-255 (8 bit image). The line AB passes through the steel fibres, the UHPC mortar and the pores. The grey value along the line ranges from 86 to 195. It can be seen that the thresholds for the fibres and the pores are around 120 and 95, respectively, and the pixels between them are mortar matrix. As demonstrated in our previous studies [23, 25], the pore volume fraction (PVF) is very sensitive to the chosen threshold. A higher threshold may falsely regard some mortar as pores and thus lead to artificially higher PVF, and vice versa. Therefore, a sensitivity analysis is carried out to determine the optimal pore threshold, which is assumed to result in the lowest slope of the PVA-threshold curve (i.e., the 2nd derivative is zero). Fig.10a and Fig.10b show the sensitivity of PVF in the 3D images to the threshold for Beam1 and Beam 2, respectively. The PVF data are fitted nicely for the two cases by fourth-order polynomials. The optimal thresholds for pores making the 2nd derivatives zero are 79 and 94, for Beam 1 and Beam 2, respectively, and the identified pores for an image slice example for each beam are shown in the central image in Fig. 11a and Fig. 11b, respectively.

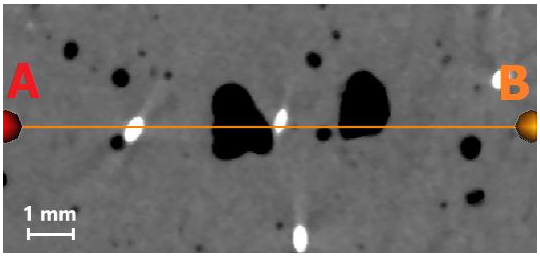

(a) Line-probe AB

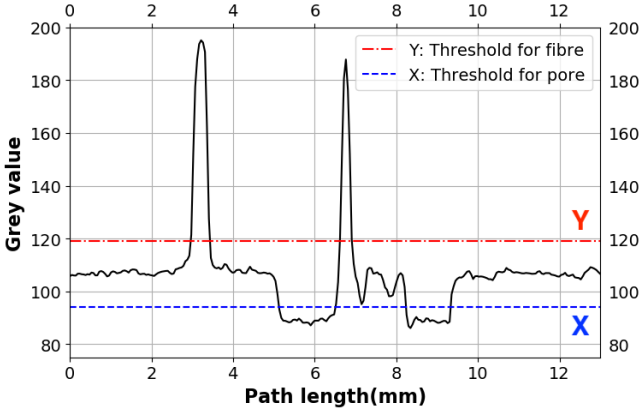

(b) Variation of grey values along line AB;

Figure 9 Initial determination of thresholds for different phases using the A-B line method for Beam 2 as an example: X (=94) and Y (=120) is the threshold for pores (dark regions) and fibres (bright white regions) respectively; the grey regions are mortar.

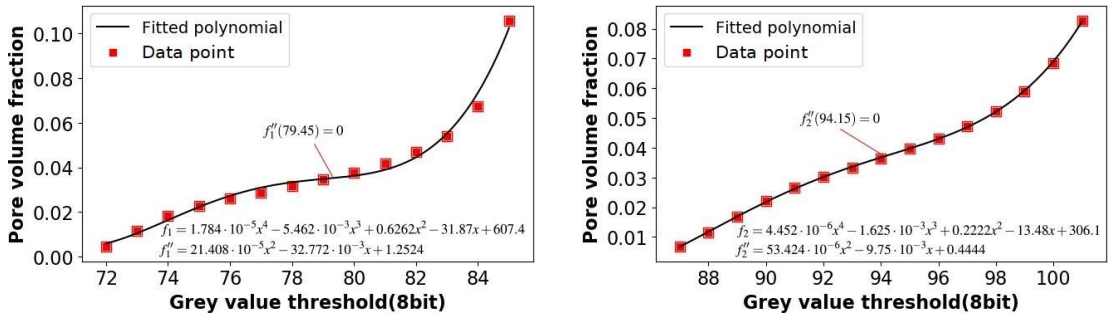

(a) Beam 1 (b) Beam 2

Figure 10 Sensitivity analysis of pore volume fraction to the threshold using fitted 4th-order polynomials: the optimal threshold is determined with zero 2nd-order derivative of the curve.

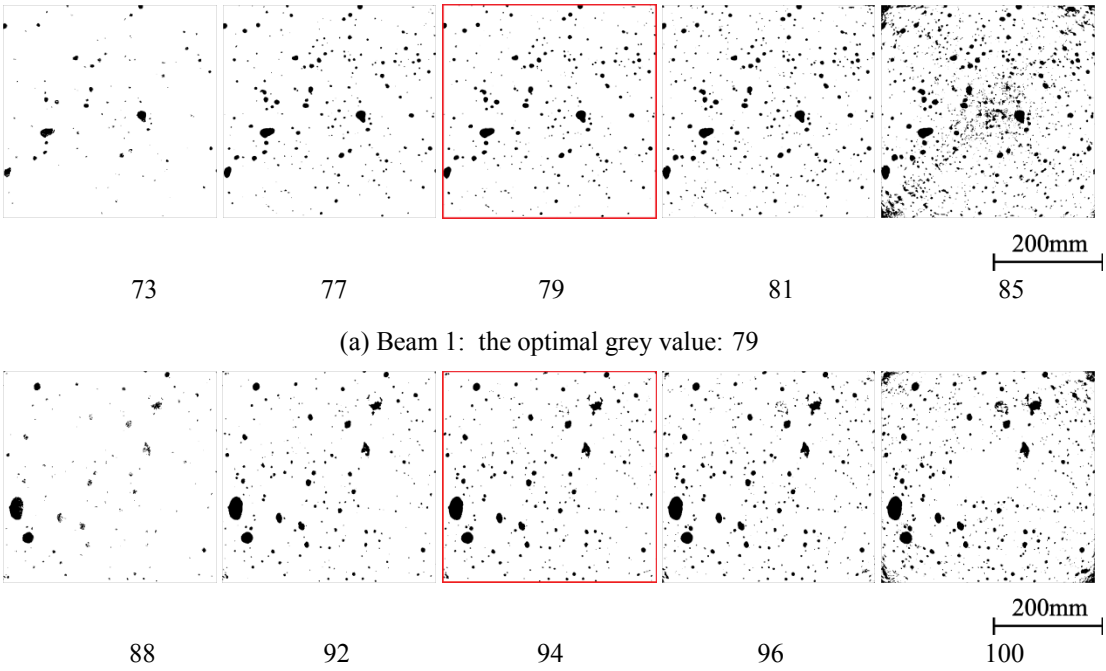

(a) Beam 1: the optimal grey value: 79

(b) Beam 2: the optimal grey value: 94

Figure 11 Pores identified using diff erent greyscale thresholds in the same image slice: the middle slice is used for segmentation with the optimal grey value for each beam.

With such thresholds, the resultant pore volume fraction is 3.45% and 3.64% for Beam1 and Beam 2, respectively. After segmentation of the pores, their connections are broken by the "Cube Opening" operation using a half-kernel size of 3pt, if a pore's voxels share at least one vertex with another pore. The number of segmented pores is 11,142 with an average volume of 0.18 mm^3 and average equivalent diameter of 700 μm for Beam1. The values are 10639, 0.19 mm^3 and 713 μm for Beam 2, respectively. Fig.12a and Fig. 12b show the 3D image of segemented pores for Beam 1 and Beam 2, respectively. It can be seen that most of the small pores are nearly spherical or ellipsoidal in shape, but those large ones are quite irregular. The

frequency distributions of pores' equivalent diameter (d_e) are plotted in Fig. 13. Among all the pores, 33.7% has d_e = 30-400 μm, 53.1% has d_e = 400-800 μm, 12.2% has d_e = 800-1600 μm and 0.9% has d_e larger than 1600 μm, respectively. The percentages for Beam 2 are 34.0%, 53.0%, 12.0% and 1.0%, resepctively. It should be noted that the pores smaller than 30μm are not detectable due to the limitation of the μXCT facility used and the specimen sizes.

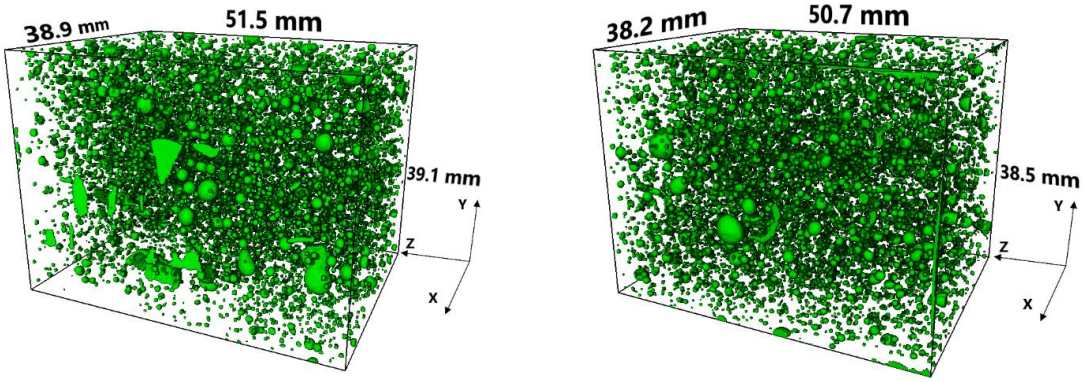

(a) Beam 1 (b) Beam 2

Figure 12 Segmented 3D images of pores for Beam 1 and Beam 2

For the steel fibres, the optimal grey value threshold should yield an average fibre diameter of all the fibres in the 3D image that is closest to the real fibre diameter 0.2 mm. The identified threshold is 99 for Beam 1 with the resultant average fibre diameter of 0.199 mm, and it is 120 for Beam 2 with the resultant average diameter of 0.191 mm. With such thresholds, the fibre volume fraction is 1.24% and 1.17% for Beam 1 and Beam 2 respectively. They are slightly higher than 1% in the mixture design, indicating the non-uniform fibre distribution during casting. Fig. 14a and Fig. 14b shows the segemented fibres for Beam 1 and Beam 2, respectively. The skeleton algorithm is then used to obtain the centre lines (skeleton) of fibres. The node position and the connectivity of fibre skeletons will be used for subsequent FE simulations.

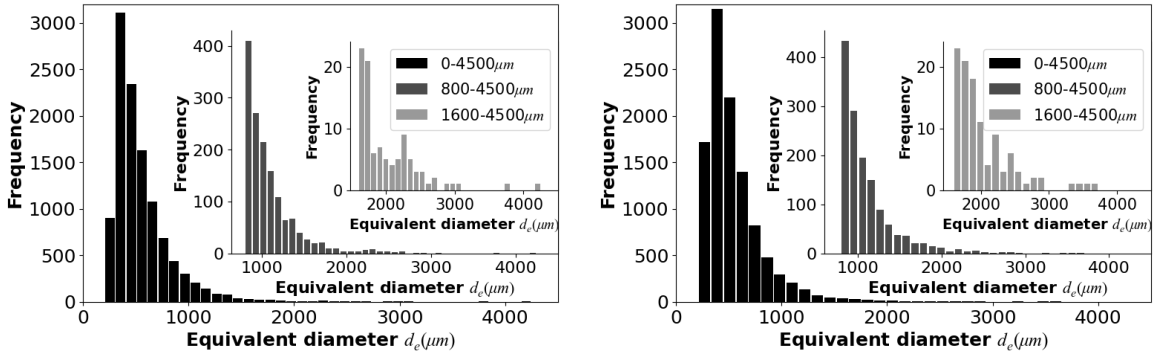

(a) Beam 1 (b) Beam 2

Figure 13 Frequency distributions of pores' equivalent diameters (d_e).

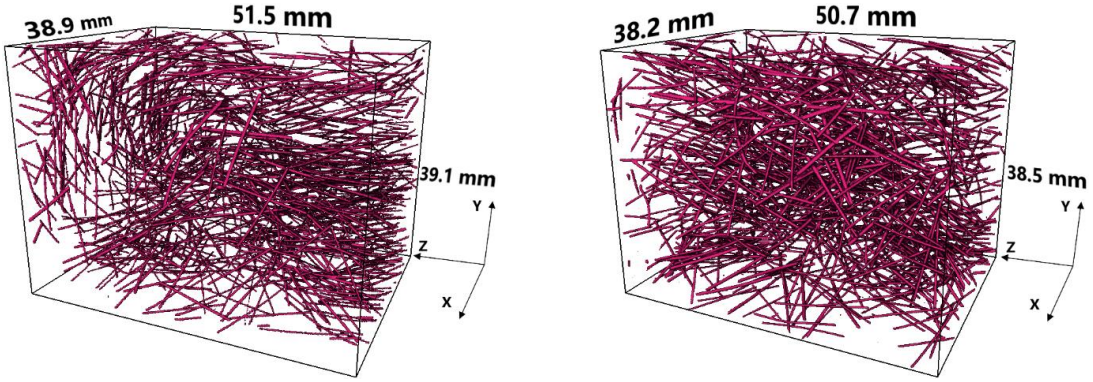

(a) Beam 1 (b) Beam 2

Figure 14 Segmented 3D images of fibres for Beam 1 and Beam 2

4. 2D Visualization and Analysis of Fracture Mechanisms

Typical 2D cropped vertical μXCT image slices in the YZ plane at different loading stages for Beam 3 are chosen to illustrate the damage and fracture mechanisms. It should be noted that the fibres in Figs 15-19 are nearly parallel to or have small angles with the YZ plane, so the measured fibre lengths, embedment lengths, end slips, and inclination angles are all approximate.

Fig.15 shows the fibre bending and crack bridging phenomena in the same image slice from three scans. The crack in the 2nd scanned image (Fig.15a) is visible but closed, due to unloading from the first peak load (see Fig. 3). As shown in Fig.15b and Fig.15c, the fibre near the bottom gradually bends as the crack propagates and widens. In the 5th scan (Fig.15c), plastic hinges appear at the fibre exit points due to highly concentrated forces from the matrix. This phenomenon is called fibre snubbing [33]. The fibres' crack bridging and restriction lead to high post-crack ductility, as shown in Fig. 3. In the zoomed views (Fig.15d-Fig.15f), the fibre's original length and orientation, the end slip and the crack width can all be measured from the images. The fibre has an origianl length of 12.41 mm, an angle with the crack path of 83.95° and an embedment length 5.62mm on the left side of the crack. The left-end slip is almost invisible throughout the loading process, but the right-end slip increases from 1.65mm to 3.73mm and the crack width increases from 1.64mm to 3.72 mm, from the 4th scan to the 6th scan (Fig. 15e and Fig. 15f). The final fibre length at the 6th scan is 12.47 mm with an overall axial strain of 0.06/12.41=0.0048, which leads an overall axial stress of 1008MPa, lower than the fibre's yield strength 2000MPa. However, from Fig. 15f it is clear that the left part of this fibre is hardly deformed. By taking this into account, the strain should be calculated based on the fibre length of 12.41-5.62=6.79mm in which the strain is 0.06/6.79=0.0088, very close to the fibre yield strain of 2000/2.1e5=0.0095. Furthermore, as the slip of the fibre's right part is considerable, it is reasonable to assume the strain in the right part of 3.30mm is negligible. In this case, the strain in the fibre length across the crack is calculated as 0.06/(12.41-5.62-3.3)=0.017>0.0095, indicating local yielding occurs. This is clearly reflected by the much thinner fibre part bridging the crack in Fig. 15f. The above image analyses demonstrate the use of progressive μXCT scannings in quantifying micro/meso-scale deformation and crack

evolution in regions of interests for fibre reinforced composites, which is beyond the capabability of conventional macroscopic tests.

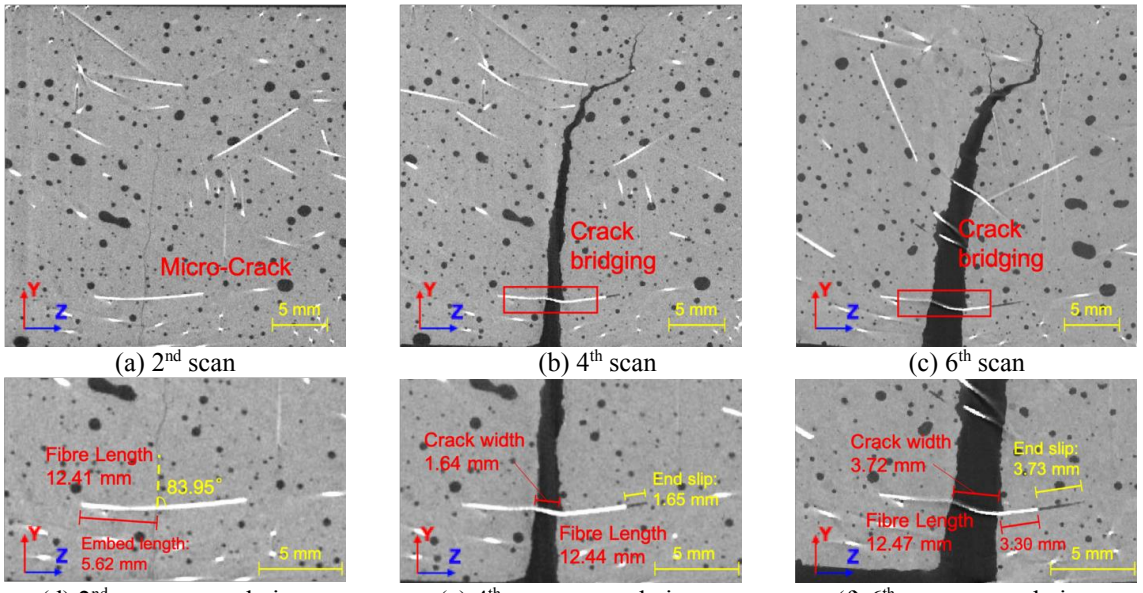

(a) 2nd scan (b) 4th scan (c) 6th scan

(d) 2nd scan zoomed view (e) 4th scan zoomed view (f) 6th scan zoomed view

Figure 15 Crack propagation, fibre bridging, bending and snubbing, and measurement of fibre length and orientation, end slips and crack width in 3 scans of Beam 3

Figs.15 and 16 reveal the fibre slip and pullout behaviour in different image slices. As shown in Fig.16a, the embedded length of the labelled fibre at the right side of the crack is 1.8 mm which is much shorter than that at the left side. The fibre inclination angle to the crack is 63.6°. In the 4th scan (Fig. 16b), fibre slip from the matrix at the right end is clearly seen and the measured slip is 1.16 mm. In the 6th scan (Fig.16c), the fibre is fully pulled out from the matrix with a slip of 1.80 mm. Because the embedment length is short at the right end, this fibre is slightly bent at the left exit point only, which is consistent with the finding in [24].

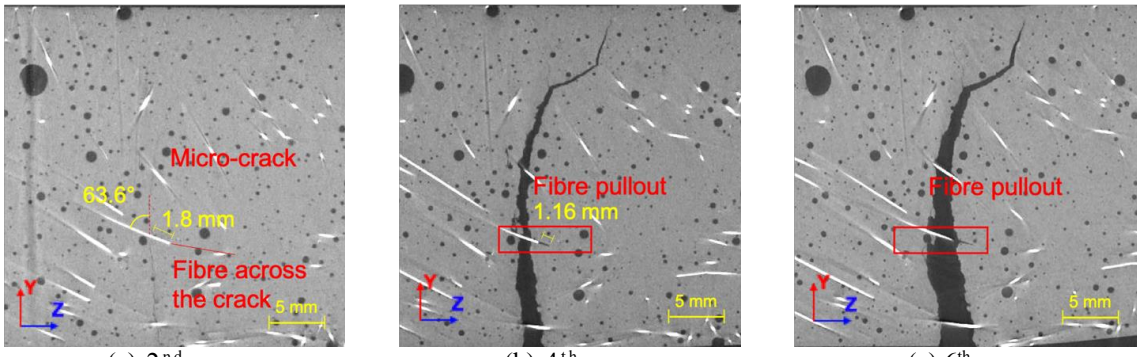

(a) 2nd scan (b) 4th scan (c) 6th scan

Figure 16 Fibre slip and pullout

Fig.17 shows the influence of a bridging fibre on the crack propagation direction (Fibre 1 as labelled in Fig.17b). When the crack reaches the bridging fibre, its propagation is stopped by the fibre, which forces the crack to propagate along its axial direction or the weaker fibre-matrix interface. Crack bifurcation also

happens because the stress state at the crack tip is significantly affected by the existence of the bridging fibre. A similar phenomenon can be observed in Fig.18, where the fibre forces the crack to propagate along the fibre-matrix interface. This so called 'pseudo-debonding' phenomenon [34] is also noted in [24] where in-situ μXCT tests of UHPFRC specimen under wedge-split loading is reported.

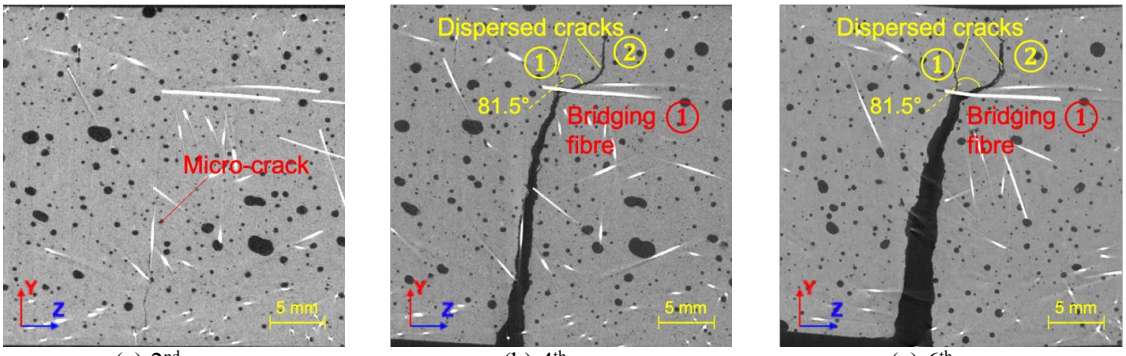

(a) 2nd scan (b) 4th scan (c) 6th scan

Figure 17 Crack direction change: bifurcation due to fibres

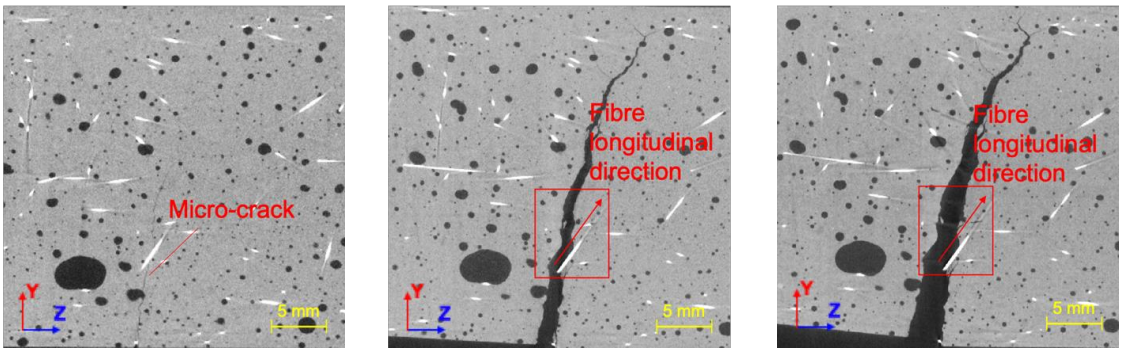

(a) 2nd scan (b) 3rd scan (c) 4th scan

Figure 18 Crack direction change due to fibres: along fibre axis direction

Fig.19 illustrated the development of cone-shaped matrix failure caused by the pulling of fibres with short embedment length, as also demonstrated by FE simulations in [33].

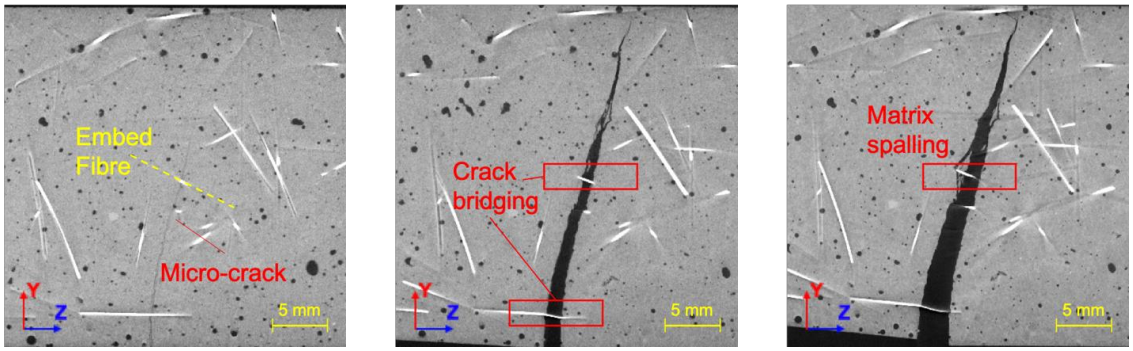

(a) 2nd scan (b) 4th scan (c) 5th scan

Figure 19 Matrix failure at three CT scans: matrix spalling due to fibre crack-bridging

Fig. 20 show the crack initiation and propagation in the bottom view (XZ plane) for Beam 3. As the

beam and loading conditions are all symmetric, the crack shoud have initiated and propagated vertically upwards but it is deviated away from the central line by more than 10mm. Since no notches exist in the beams tested in this study, such deviation should mainly caused by non-symmetric distribution of internal fibres or pores. Detailed 3D views of pores with different sizes at the 3rd scan for Beam 3 are shown in Fig. 21, using a grey threshold of 66 for the pores. Zoomed views near the bottom are also shown in Figs 21d-f. Comparing Fig. 21e and Fig. 21f indicates that although there are two pores> 0.36mm^3 near the central line, they are much smaller than the two pores >1.08mm^3 near the crack. Therefore, it is reasonable to infer that the on/near-surface big pores have significant effects on the crack initiation location, probably due to the stress concentration caused by their existance. This also happens in Beam 1 and Beam 2, as will be shown in Section 5.4.3. This leads to the inclined macroscopic cracks on the elevation views for all three beams (Fig.2).

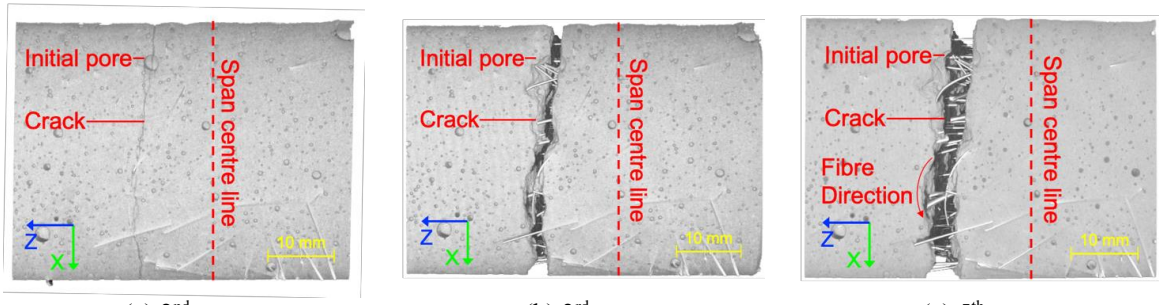

(a) 2nd scan (b) 3rd scan (c) 5th scan

Figure 20: The influence of bottom near-surface pores on the crack initiation position

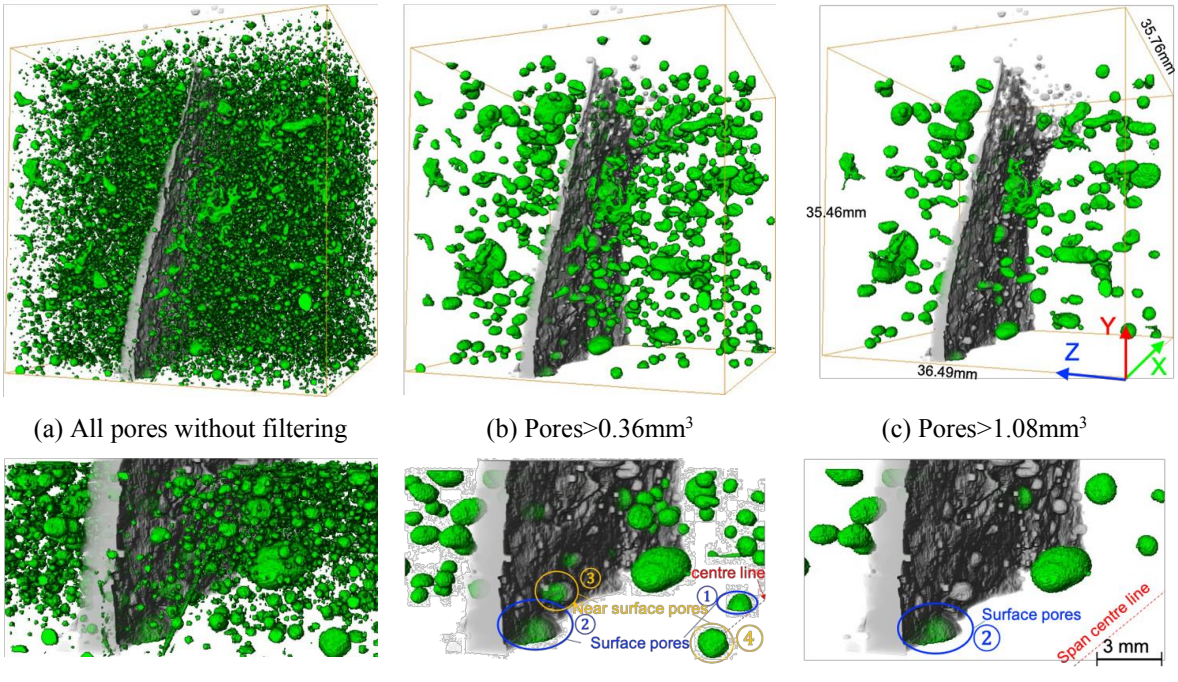

(a) All pores without filtering (b) Pores>0.36mm^3 (c) Pores>1.08mm^3

(d) Zoomed view of all pores (e) Zoomed view with pores>0.36mm^3 (f) Zoomed view of pores>1.08mm^3

Figure 21: The influence of bottom near-surface pores on the crack shape (3D view)

5. Numerical Simulations and Validation

Two-scale FE models are built for Beam 1 and Beam 2 with nonlinear damage and fracture processes until structural failure simulated and compared with the test results. The FE mesh for each beam consists of two parts: a fine mesoscale mesh consisting of fibres, mortar and pores, with a general elemental size of 1mm in the central region converted from the segmeneted 3D μXCT image (Fig. 12 and Fig. 14), and coarse meshes with elemental size of 10 mm on the two sides with homogenised material properties of UHPFRC. Analytical rigid bodies are used to model the supporting and loading steel rods, with surface to surface contact simulated between them and the beam. The whole mesh, the central mesh, and the central mesh with fibres highlighted, are shown in Figs. 22a-c for Beam 1. There are 80,263 nodes and 431,737 four-noded tetrahedron elements in total. The mesh for Beam 2 is similar. The models with the same meshes but without fibres are also simulated for comparison. All the simulations are conducted in ABAQUS using the implicit solver with displacement control.

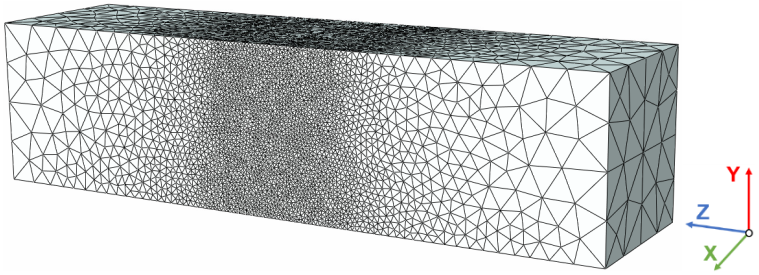

(a) The whole mesh

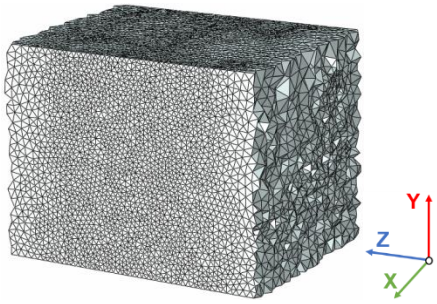

(b) The central mesh

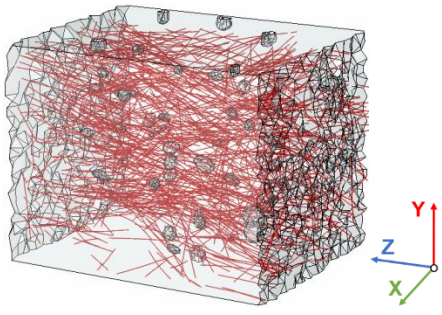

(c) The central interior mesh

Fig. 22 Two-scale finite element mesh for Beam 1

5.1 Mesh Generation

Modelling all the pores (over 10,000) as small as 3.48E-5 mm^3 in Fig. 12 and Fig. 14 would lead to extremely fine local meshes with gigantic number of degrees of freedom. To limit the computational cost as well as to capture key mechanisms, only the 37 and 57 pores larger than 3.0 mm^3 are included in the FE models, as shown in Fig. 23a and Fig. 23b for Beam 1 and Beam 2, respectively. Ignoring smaller pores

would make negligible difference to the crack path and load-carrying capacity, when there was one dominant crack in the specimens, as demonstrated in our previous CT-image based simulations of concrete [26-29]. It can be seen that most of the pores are irregular in shape. In addition, Fig. 20 and Fig. 21 shows that the pores on the surfaces signifcantly affect the crack initiation and propagation. Therefore, the pores are modelled with polyhedrons defined by surface segments after smoothing, as shown in Fig. 24, rather than spheres assumed by other studies such as [19].

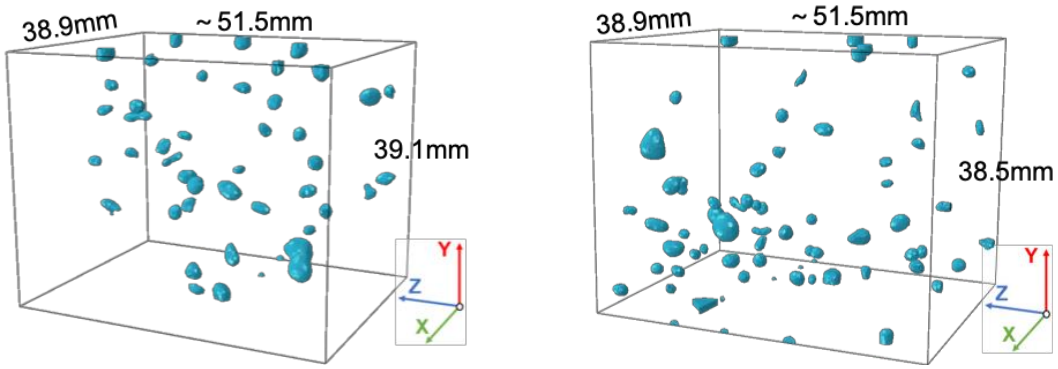

(a) Beam 1 (b) Beam 2

Fig. 23 Pores used in FE models

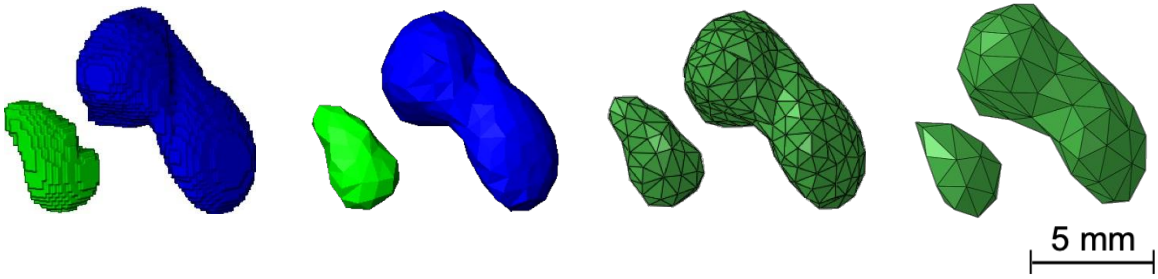

(a) Original μXCT image (b) After surface smoothing (c) Surface mesh (d) Simplified mesh

Figure 24: Meshing irregular pores from μXCT image to surface segments

A Python code (with Gmsh SDK API [35]) is then developed to conduct a Boolean operation to remove the polyhedrons representing pores. The 3D Delaney algorithm is then used to generate the mesh of mortar with tetrahedral elements, followed by mesh quality optimisation using the Netgen algorithm [35].

The steel fibres are modelled by two-noded truss elements and are embedded into the mortar mesh, with the fibre-matrix interaction simulated indirectly by the approximate method presented in section 5.3. The length of fibre elements is about 1 mm, short enough to simulate bent fibre segments during casting and is also consistent with the surrounding mortar elements' size. The nodes of the fibre elements are not necessarily coincident with those of surrounding mortar elements, i.e., non-conforming; this simplifies mesh generation considerably.

5.2 *Constitutive Models and Parameters for Fibres and Mortar*

The concrete damage plasticity (CDP) constitutive law in ABAQUS is widely used for modelling the damage behaviour of concrete, mortar and FRC[1, 26]. In this study, the CDP model is used to model the mortar in the central region as well as the homogenised UHPFRC material in other regions. The basic material parameters of the homogenised UHPFRC, the mortar (without fibres) and the fibres are listed in Table 2. They are from the compressive cube tests, calculated according to relevant equations in [36] and estimation.

Table 2: Basic material properties used in FE simulations

UHPFRC (with fibres embedded) on two sides					
E_0 (MPa)	Density (kg/m^3)	v	f_c' (MPa)	f_t (MPa)	G_f (N·mm)
40554	2000	0.2	120	11	0.5
UHPC mortar (without fibre) in the centre					
E_0 (MPa)	Density (kg/m^3)	v	f_c' (MPa)	f_t (MPa)	G_f (N·mm)
39048	2000	0.2	110	7	0.05
Steel fibres in the centre					
E_0 (MPa)	Density (kg/m^3)	v	f_y (MPa)	f_u (MPa)	ε_u (ultimate strain)
200,000	7850	0.3	2000	2400	0.2

For both mortar and UHPFRC, the RPC200 uniaxial compressive stress-strain curve proposed by Ma [37] is used to describe the pre-peak hardening curve and the post-peak softening curve in the CDP models:

$$y = \begin{cases} Ax + (5-4A)x^4 + (3A-4)x^5 & (0 \le x \le 1) \\ \frac{x}{\alpha(x-1)^2+x} & (x \ge 1) \end{cases} \quad (1)$$

where the parameter x is the ratio between the strain (ε) and the strain at the peak stress (ε_c); y is the ratio between the stress(σ) and the strength f_c'; A is the ratio of the initial elastic modulus E_0 to the tangent stiffness E_p at the peak load. α is a coefficient describing the descending branch of the curve. According to the experiments in [37], the optimal ranges of A and α are: $1.1 \le A \le 1.4$, and $6.0 \le \alpha \le 10.0$. In this study, α is assumed to be 6.0. The value of A is calculated using an empirical equation [38]:

$$\mathrm{A} = \frac{11.788 f_c' + 2522.5}{17.2 f_c' + 836.4} \quad for \quad 80\mathrm{MPa} \le f_c' \le 220\mathrm{MPa} \quad (2)$$

The elastic modulus E_0 is calculated as:

$$E_0 = \frac{10^3}{0.0142 + 1.255/f_c'} \quad (3)$$

The traction-crack opening displacement softening relationship proposed by Hordijk [39] is used to model the tensile behaviour of mortar and UHPFRC, in order to minimize the mesh dependence of results:

$$\frac{\sigma_t}{f_t} = \left[1 + \left(3\frac{w}{w_0}\right)^3\right] e^{\left(-6.93\frac{w}{w_0}\right)} - 10\frac{w}{w_0} e^{(-6.93)} \quad (4)$$

where w_0 is the crack opening displacement when the tensile stress becomes zero and it is calculated as:

$$w_0 = 5.4\frac{G_f}{f_t} \quad (5)$$

The CDP model requires the definition of other five plasticity parameters, i.e. , the dilation angle the flow potential eccentricity, the ratio of initial bi-axial compressive yield stress to initial uni-axial compressive yield stress, the ratio of the second stress invariant on the tensile meridian to that on the compressive meridian, and the viscosity parameter. 45°, 0.1, 1.16, 0.667 and 3e-6 are used in this study.

5.3 Indirect Modelling of Fibre-matrix Interfacial Bond-slip

The nonlinear bond-slip softening behaviour of fibre-mortar interfaces plays a key role in the damage and fracture mechanisms and the load-carrying capacities in the UHPFRC specimens, as demonstrated by a 2D discrete-continuum coupled model developed in our previous study [40]. However, extending such a model to 3D with randomly distributed fibres is very challening and still underway. Instead, for simplicity of meshing in this study, the fibre elements are perfectly bonded to the mortar elements and consequently, the fibre-mortar interfacial bond-slip behaviour is modelled indirectly, using the following method (similar to that in [41]).

The equivalent interfacial shear stress $\tau(s)$ is defined using the fibre pull-out load-displacement relationship as

$$\tau(s) = \frac{P(s)}{\pi d_f L_E} = \tau_0 + \tau_H \times \frac{s}{L_E} + \tau_A(s) \quad (6)$$

where s is the pull-out displacement, L_E is the effective length of the fibre (assumed as half fibre length for simplicity), and d_f is the fibre perimeter. τ_H is the slip-hardening shear stress and ranges from 1 to 32 MPa for hooked end or twist fibres. No slip-hardening behaviour is expected for straight smooth fibres used in this study. τ_0 is the average static shear stress when the fibre is fully debonded from the mortar, and it is approximated as a ratio to the mortar's tensile strength:

$$\tau_0 \approx \frac{2}{3} f_t \quad (7)$$

τ_0=4.67MPa in this study.

$\tau_A(s)$ is the equivalent shear stress associated with the anchorage force Q:

$$\tau_A(s) = \frac{Q}{\pi d_f (L_E - s)} \quad (8)$$

From Eqs (6)-(8), the equivalent axial stress-pullout displacement relation (σ_f-s) of fibres is obtained as:

$$\sigma_f(s) = \frac{\tau(s) d_f \pi (L_E - s)}{A_f} \quad (9)$$

The corresponding stress-strain relationship ($\sigma_f - \varepsilon_f$) is:

$$\sigma_f(\varepsilon_f) = \frac{\tau(\varepsilon_f) d_f \pi L_E (1 - \varepsilon_f)}{A_f} \quad (10)$$

with

$$\varepsilon_f = s / L_E \quad (11)$$

Parameters Q, τ_H and the initial ascending stiffness E_{init} are dependent on the fibre inclination angle

relative to the crack surface. The influences of Q and τ_H are shown in Fig.25a and Fig. 25b, respectively. A higher Q moves the curve up without changing its shape, and a higher τ_H not only moves the curve up but changes its shape from concavity to convexity. A positive τ_H leads to a convex curve indicating a slip-hardening behaviour while a negative value results in a concave curve with a slip-softening behaviour.

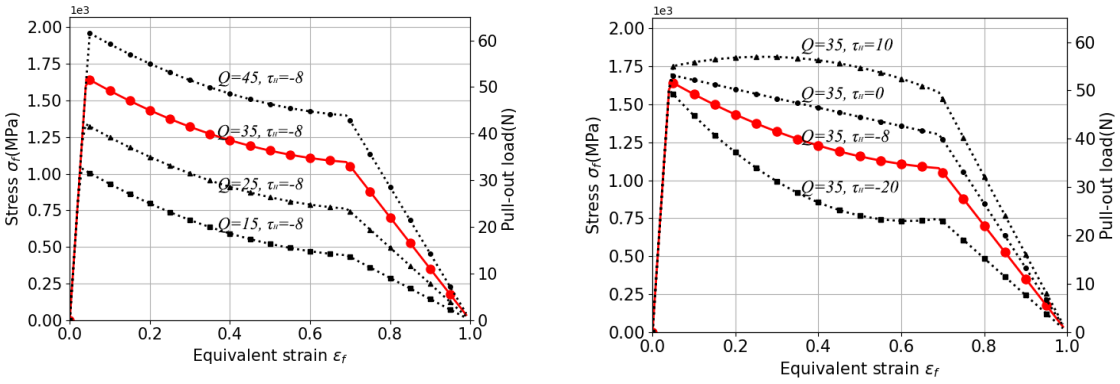

(a) Q (b) τ_H

Figure 25 Parametric studies of Q and τ_H: Q determines the height of the curve and τ_H determines the concavity/convexity of the curve

For randomly distributed fibres, it is impossible to have a one-to-one σ_f- ε_f relationship for every fibre inclination angle and embedment length. Therefore, the σ_f- ε_f relationships from the pull-out tests in [42] with the angle of 0°, 15°, 30°, 45° and 60° are assigned to the fibre elements with an inclination angles ranging from 0°-7.5°, 7.5°-22.5°, 22.5°-37.5°, 37.5°-52.5°, and 52.5°-67.5°, respectively. The fibres with the inclination angle from 67.5°-90° are assumed to be perfectly bonded with the mortar and they are modelled by the elastoplastic constitutive law with material properties given in Table.2. Fig.26 shows the fitted curves, compared with original experimental data, using Eqs (6)-(10) with the parameters listed in Table 3 for the five inclination angle groups.

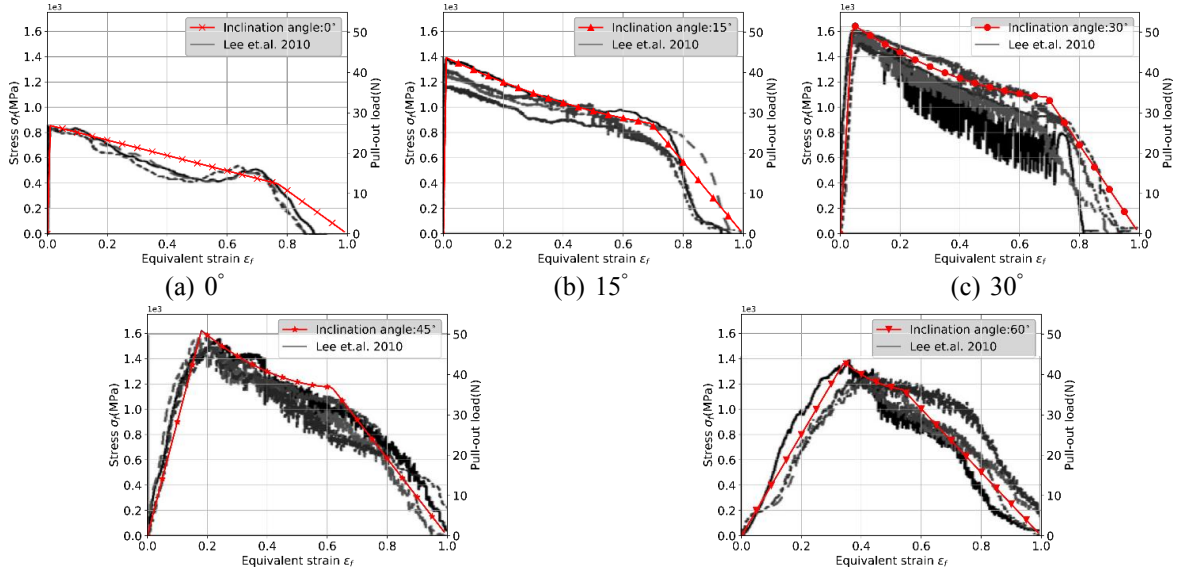

(a) 0° (b) 15° (c) 30°

(d) 45° (e) 60°

Figure 26 Equivalent fibre stress-strain curves for five inclination angles: fitted using Eq.(6)-Eq.(10) with parameters listed in Table 3

Table 3: Parameters for fitting the equivalent fibre stress-strain curves

Inclination angle	E_{init} (MPa)	τ_H (MPa)	Q (MPa)
0°	1e5	0	8
15°	1e5	-4	25
30°	4e4	-8	35
45°	2e4	-16	45
60°	1e4	-32	60

Fig.27a and Fig. 27b shows the histogram of fibre element inclination angle for Beam 1 and Beam 2, respectively. For both beams, the inclination angle of most fibres ranges 52.5°-90°, and there are about 700 more fibre elements in Beam 2 in this angle range than in Beam 1. This may contribute to the higher post-peak load-carrying capacity for Beam 2 (Fig. 3).

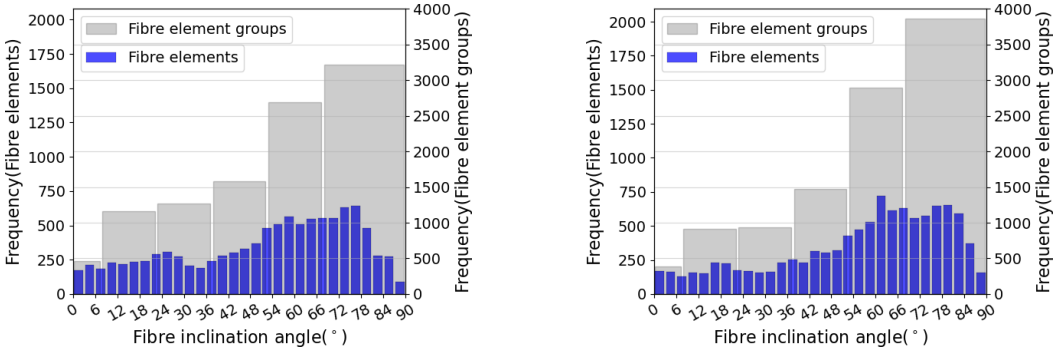

(a) Beam 1 (b) Beam 2

Figure 27 Histograms of fibre element inclination angles in six fibre inclination ranges.

5.4 Simulation Results and Discussion

5.4.1 Comparison of crack paths

Fig.28 and Fig.29 compare the predicted cracks in three views (front, back and bottom) from the FE modelling and in the tested beam, for Beam 1 and Beam 2, respectively. The simulated cracks are represented by the mortar elements with tensile damage index DAMAGET ≥0.4. Both the crack paths and shapes are highly similar.

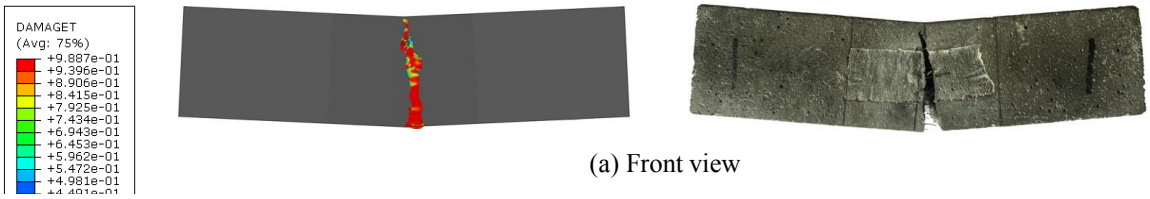

(a) Front view

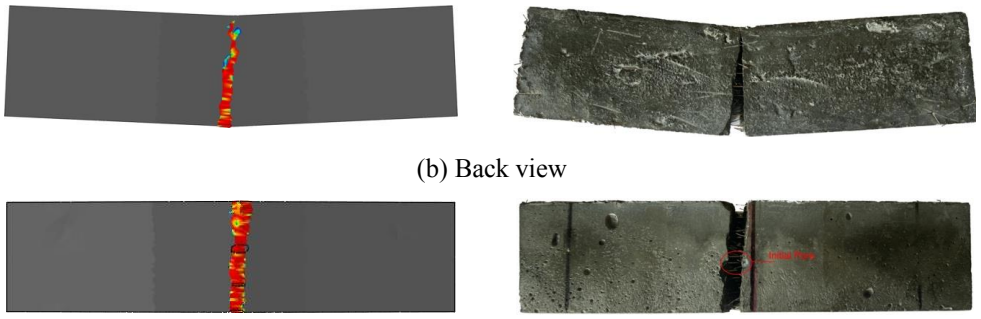

(b) Back view

(c) Bottom view

Figure 28 Comparison of simulated and tested cracks of Beam 1

349

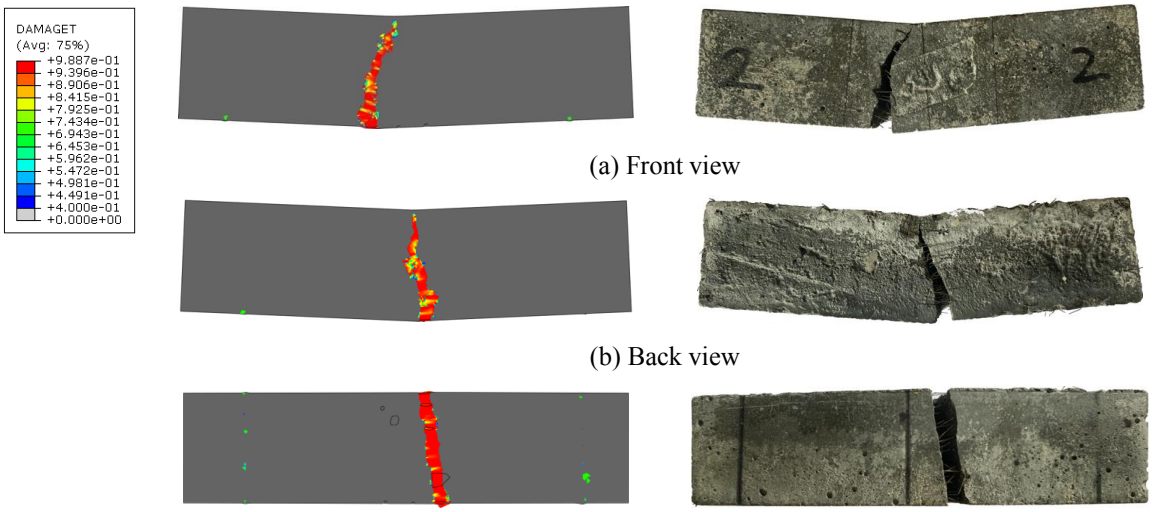

(a) Front view

(b) Back view

(c) Bottom view

Figure 29 Comparison of simulated and tested cracks of Beam 2

350 ***5.4.2 Comparison of load-displacement curves***

351 Fig. 30a compares the load-displacement curves obtained from the tests and simulations for both
352 UHPFRC beams. Good overall agreement is achieved as well as the cracking load and the maximum
353 bridging load. However, the initial parts of simulation curves are stiffer than the corresponding experimental
354 parts. This may be caused by the machine compliance, which is unknown and neglected in the FE
355 simulations. The descending parts of the simulated curves are steeper than those of the experimental curves,
356 probably because the fibre-mortar interfacial bond-slip behaviour is modelled by the approximate method in
357 Section.5.3. Fig. 30b compares the load-displacement curves from the simulations of UHPFRC beams and
358 UHPC beams (without fibres). It can be seen that although the cracking loads (the first peak loads) of the
359 models without fibres are only slightly lower than those of the models without fibres, the models without
360 fibres are very brittle. On the contrary, the models with fibres are very ductile, demonstrating the fibres'
361 strong crack bridging effects.

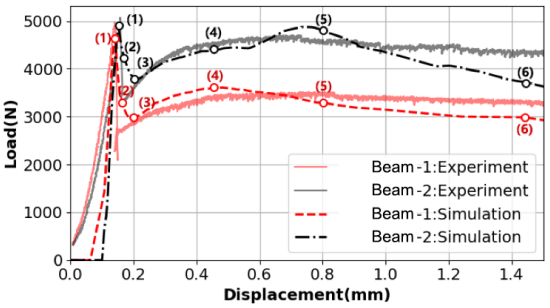

(a) UHPFRC beams from experiments and simulations

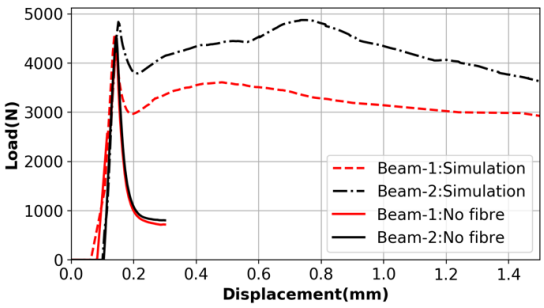

(b) UHPFRC and UHPC beams from simulations

Figure 30 Comparison of load-displacement curves

5.4.3 3D Crack evolution and comparison with μXCT images

Fig. 31 and Fig. 32 shows the 3D cracks represented by mortar elements with DAMAGET ≥0.4 for Beam 1 and Beam 2, respectively, at six load steps as marked in Fig.30a. It can be seen that the crack initiates at the areas with densely-distributed pores at the beam bottom (Fig. 31a and Fig. 32b), as reflected by the deviation of crack paths from the central lines of both beams in the test. The crack stops propagating at early stage (point 4 in Fig. 30a) but keeps widening thereafter without losing strength. This again demonstrates the strong crack-bridging effects of steel fibres on structural ductility. It can also be seen that the crack initiates later in Beam 2 than in Beam 1, although there are more pores near the bottom surface in Beam 2. This may be again due to the more fibres in Beam 2, which exert higher constraints against crack initiation.

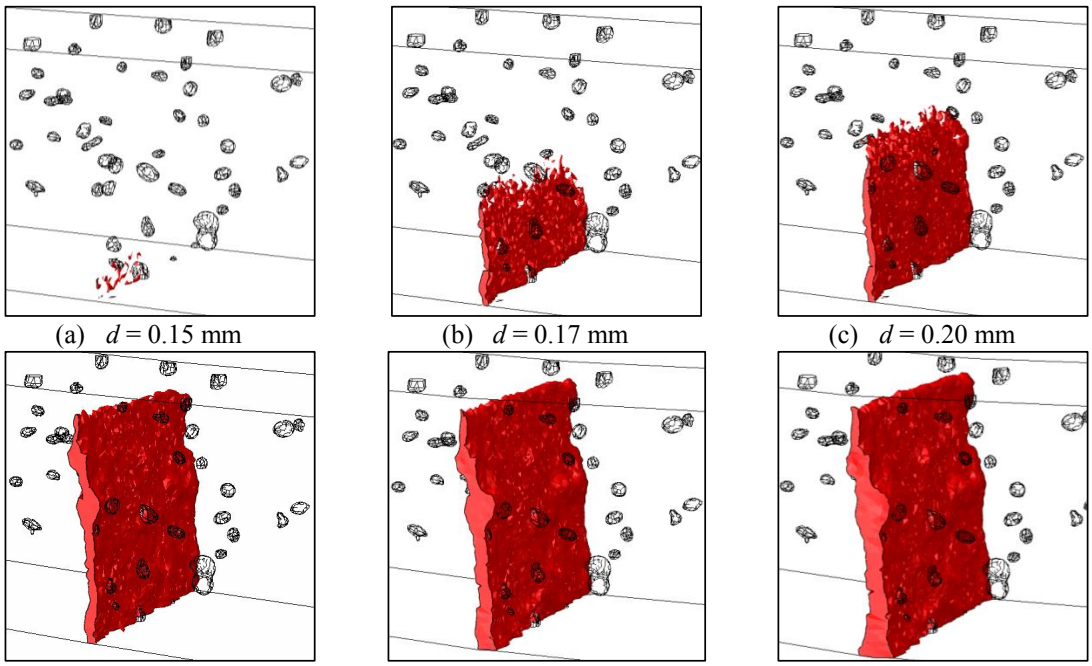

(a) d = 0.15 mm (b) d = 0.17 mm (c) d = 0.20 mm

(d) d =0.45 (e) d = 0.80 mm (f) d = 1.45 mm

Figure 31 Simulated 3D crack evolution of Beam 1 in six loading steps: the cracks are represented by mortar elements with DAMAGET>0.4

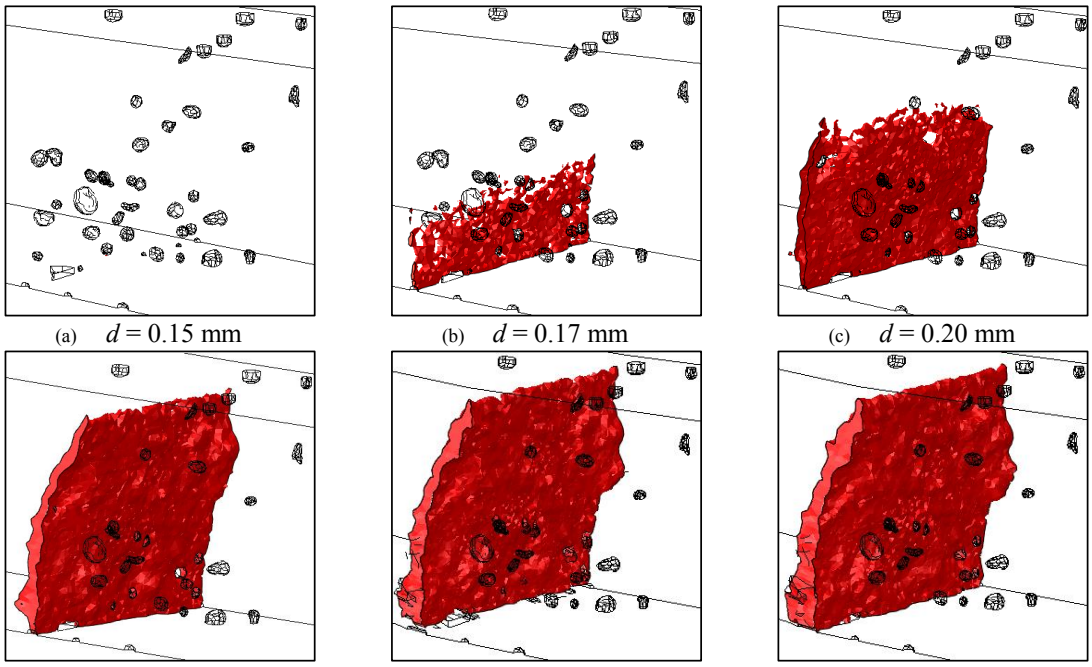

(a) d = 0.15 mm (b) d = 0.17 mm (c) d = 0.20 mm

(a) d = 0.45 mm (b) d = 0.80 mm (c) d = 1.45 mm

Figure 32 3D Simulated crack evolution of Beam 2 in six loading steps: the cracks are represented by mortar elements with DAMAGET>0.4

The simulated final 3D crack surfaces are compared with the μXCT images in Fig. 33 and Fig. 34, respectively, with excellent qualitative agreement. The very uneven crack surfaces demonstrate the significant effects of micro/meso-structures near the crack paths, especially the distribution of pores and orientation of fibres (see below). On the contrary, the models without fibres lead to nearly vertical crack paths and smooth crack surfaces, which are not shown here.

(a) XCT image (b) Simulated

Fig. 33 Comparison of crack path and surfaces of Beam 1

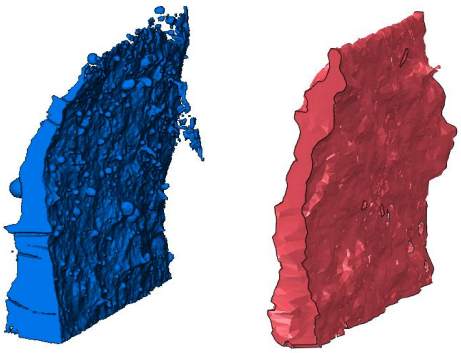

(a) XCT image (b) Simulated

Fig. 34 Comparison of crack path and surfaces of Beam 2

5.4.4 Evolution of fibre stress and deformation

Fig. 35 and Fig. 36 shows the stress evolution in the crack-bridging fibres in Beam 1 and Beam 2, respectively. It can be seen that when the crack initiates, some fibres experience about 150-300 MPa stress already, indicating the fibre constraining effects on crack initiation. The stress level in some fibres increases to about 900 MPa before the second hardening stage begins (Fig. 35c and Fig. 36c). At the second peak with displacement of 0.45 mm, the stress in a few fibres approaches the yield strength (2000 MPa). The crack keeps widening afterwards and the stress in more and more fibres exceeds the yield strength. At the final stage (Fig. 35f and Fig. 36f), many fibres have reached the fibre tensile strength 2400 MPa. This demonstrates again the strong crack-bridging and constraint effects of steel fibres. It should be noted that the present model is not capable of accurately predicting the true stress in the fibres because of the indirect simulation of fibre-mortar interfacial bond-slip behaviour, and the stress values above (and those in Fig. 35 and Fig. 36) are only rough estimations.

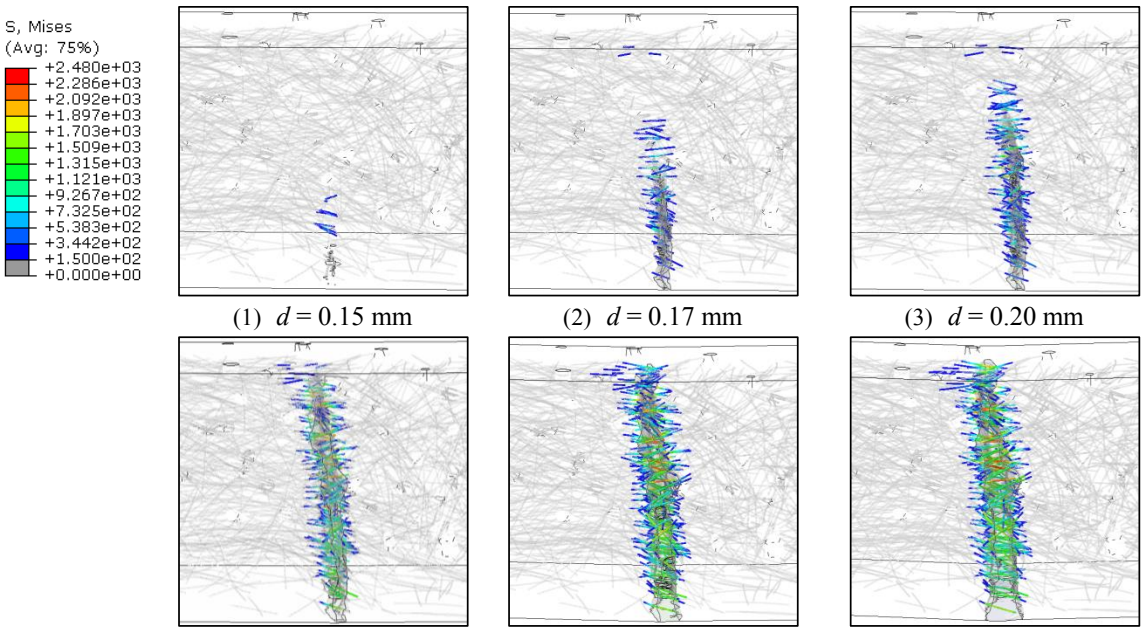

(1) $d = 0.15$ mm (2) $d = 0.17$ mm (3) $d = 0.20$ mm

(4) $d = 0.45$ mm (5) $d = 0.80$ mm (6) $d = 1.45$ mm

Fig. 35 Simulated equivalent stress evolution in crack-crossing fibres of Beam 1

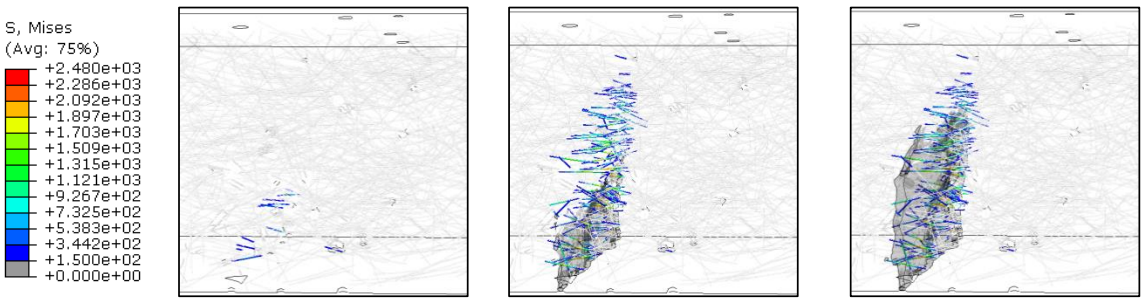

(1) $d = 0.15$ mm (2) $d = 0.17$ mm (3) $d = 0.20$ mm

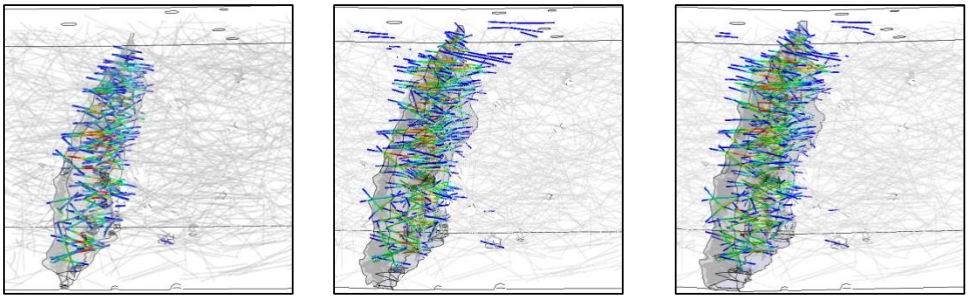

(4) d = 0.45 mm (5) d = 0.80 mm (6) d = 1.45 mm

(a) Beam 2

Fig. 36 Simulated equivalent stress evolution in crack-crossing fibres of Beam 2

Fig. 37 and Fig. 38 shows the crack-crossing fibres, with those highly deformed fibre segments highlighted, for Beam 1 and Beam 2, respectively, with comparison with the corresponding μXCT images. It can be seen that the deformed fibres are highly similar, indicating the effectiveness of the image-based models. There are 292 and 325 fibres across the crack for Beam 1 and Beam 2, respectively. This again explains why Beam 2 has higher post-peak strength and toughness than Beam 1.

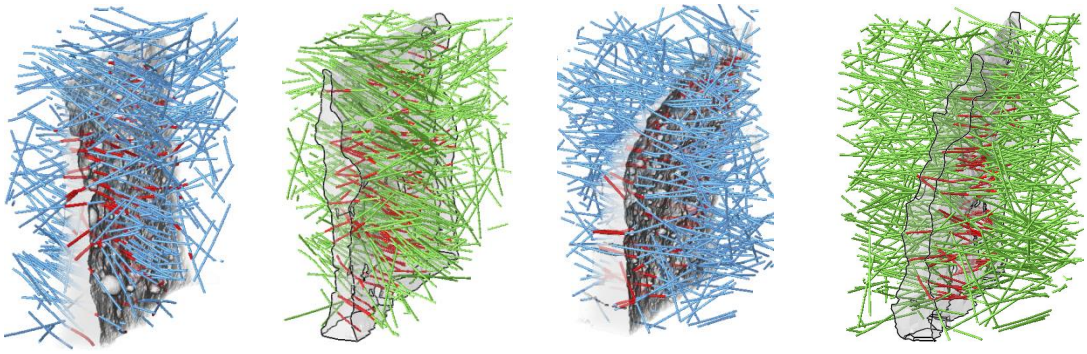

(a) XCT image (b) Simulated

Figure 37 Deformation of crack-crossing fibres: Beam 1 (severely deformed fibres in red)

(a) XCT image (b) Simulated

Figure 38 Deformation of crack-crossing fibres: Beam 2 (severely deformed fibres in red)

6. Conclusions

(1) Ex-situ micro X-ray computed tomography tests of three UHPFRC beams subjected to continuous and load-unload cyclic three-point bending have been carried out. The distribution, number, orientation and dimension of pores and fibres are statistically quantified by development of a detailed image processing procedure and a new approach for determination of accurate pore segmentation thresholds;

(2) Various micro/meso-scale deformation and failure mechanisms of UHPFRC are captured by the μXCT images, such as the mortar spalling, fibres' bending, constraining, bridging and dispersion of cracks, and fibre-mortar interfacial slip and debonding. The fibre elongation and end slips can be

accurately measured for calculation of fibre strain. It is found local yielding can occur in the fibre bridging the main crack, and the on/near-surface big pores have significant effects on the crack initiation position;

(3) 3D μXCT image-based meso-scale FE models are built with pores and fibres modelled explicitly, and they are well validated by the ex-situ μXCT images, in terms of load-displacement curves, crack paths and surfaces, and deformation of fibres. The simulations have confirmed the significant effects of fibre orientation and pore distribution on crack initiation and propagation as found in the tests. Although the fibre-mortar interfaces are not simulated directly, such meso-scale models are capable of reproducing the global fracture behaviour and structural responses of the UHPFRC beams within reasonable computational times, and thus can be used for optimisation of material-level features such as the dimensions, orientations and distributions of pores and fibres; and

(4) This study demonstrates the powerful synergy between ex-situ μXCT tests and image-based FE modelling in elucidating fundamental deformation and failure mechanisms of complicated composite materials such as UHPFRC, which cannot be rivalled by macroscopic tests and homogenisation-based numerical simulations.

7. Acknowledgements

This study is funded by Key Research and Development Programme of Hubei Province (No. 2020BAB052), Sino-German Center for Research Promotion (Mobility Programme No. M-0172), and National Natural Science Foundation of China (No. 51974202 and No. 51779222).

References

[1] Mahmud GH, Yang ZJ, Hassan AM. Experimental and numerical studies of size effects of Ultra High Performance Steel Fibre Reinforced Concrete (UHPFRC) beams. Construction and Building Materials. 2013;48:1027-34.

[2] Sun XK, Diao B, Ye YH, Geng J, Ma LY. Experiment on Mechanical Properties of Ultra-high Performance Reinforced Concrete with Hybrid-fiber. Journal of Architecture and Civil Engineering. 2012.

[3] Habel K, Viviani M, Denarié E, Brühwiler E. Development of the mechanical properties of an ultra-high performance fiber reinforced concrete (UHPFRC). Cement and Concrete Research. 2006;36:1362-70.

[4] Rossi P, Arca A, Parant E, Fakhri P. Bending and compressive behaviours of a new cement composite. Cement and Concrete Research. 2005;35:27-33.

[5] Magureanu C, Sosa I, Negrutiu C, Heghes B. Mechanical properties and durability of ultra-high-performance concrete. ACI Materials Journal. 2012;109:177.

[6] Le TT. Ultra high performance fibre reinforced concrete paving flags: University of Liverpool; 2008.

[7] Weiliang J, Yuxi Z. State of the art on durability of concrete structures. Journal of Zhejiang University (Engineering Science). 2002;36:371-80.

[8] Luo X, Sun W, Chan SY. Characteristics of high-performance steel fiber-reinforced concrete subject to high velocity impact. Cement and Concrete Research. 2000;30:907-14.

[9] Rong ZD, Sun W, Zhang YS, She W. Study on the Characteristics of Ultra-High Performance Steel Fiber Reinforced Concrete under the Second Explosion. Journal of North China Institute of Water Conservancy and Hydroelectric Power. 2012.

[10] Habel K, Gauvreau P. Response of ultra-high performance fiber reinforced concrete (UHPFRC) to impact and static loading. Cement and Concrete Composites. 2008;30:938-46.

[11] Maire E, Withers PJ. Quantitative X-ray tomography. International materials reviews. 2014;59:1-43.

[12] Terada K, Miura T, Kikuchi N. Digital image-based modeling applied to the homogenization analysis of composite materials. Computational Mechanics. 1997;20:331-46.

[13] Sharma R, Mahajan P, Mittal RK. Elastic modulus of 3D carbon/carbon composite using image-based finite element simulations and experiments. Composite Structures. 2013;98:69-78.

[14] Saucedo-Mora L, Marrow T. Multi-scale damage modelling in a ceramic matrix composite using a finite-element microstructure meshfree methodology. Philosophical Transactions of the Royal Society A: Mathematical, Physical and Engineering Sciences. 2016;374:20150276.

[15] Yang ZJ, Ren WY, Sharma R, McDonald S, Mostafavi M, Vertyagina Y, et al. In-situ X-ray computed tomography characterisation of 3D fracture evolution and image-based numerical homogenisation of concrete. Cement and Concrete Composites. 2017;75:74-83.

[16] Nguyen T, Ghazlan A, Kashani A, Bordas S, Ngo T. 3D meso-scale modelling of foamed concrete based on X-ray computed tomography. Construction and Building Materials. 2018;188:583-98.

[17] Trainor KJ, Foust BW, Landis EN. Measurement of energy dissipation mechanisms in fracture of fiber-reinforced ultrahigh-strength cement-based composites. Journal of engineering mechanics. 2013;139:771-9.

[18] Suuronen J-P, Kallonen A, Eik M, Puttonen J, Serimaa R, Herrmann H. Analysis of short fibres orientation in steel fibre-reinforced concrete (SFRC) by X-ray tomography. Journal of Materials Science. 2013;48:1358-67.

[19] Barnett SJ, Lataste J-F, Parry T, Millard SG, Soutsos MN. Assessment of fibre orientation in ultra high

performance fibre reinforced concrete and its effect on flexural strength. Materials and Structures. 2010;43:1009-23.

[20] Ríos JD, Leiva C, Ariza MP, Seitl S, Cifuentes H. Analysis of the tensile fracture properties of ultra-high-strength fiber-reinforced concrete with different types of steel fibers by X-ray tomography. Materials & Design. 2019;165:107582.

[21] Ríos JD, Mínguez J, Martínez-De La Concha A, Vicente MÁ, Cifuentes H. Microstructural analyses of the addition of PP fibres on the fracture properties of high-strength self-compacting concrete by X-ray computed tomography. Construction and Building Materials. 2020;261:120499.

[22] Skarżyński Ł. Mechanical and radiation shielding properties of concrete reinforced with boron-basalt fibers using Digital Image Correlation and X-ray micro-computed tomography. Construction and Building Materials. 2020;255:119252.

[23] Qsymah A, Sharma R, Yang ZJ, Margetts L, Mummery P. Micro X-ray computed tomography image-based two-scale homogenisation of ultra high performance fibre reinforced concrete. Construction and Building Materials. 2017;130:230-40.

[24] Yang ZJ, Qsymah A, Peng YZ, Margetts L, Sharma R. 4D characterisation of damage and fracture mechanisms of ultra high performance fibre reinforced concrete by in-situ micro X-Ray computed tomography tests. Cement and Concrete Composites. 2020;106:103473.

[25] McDonald SA, Dedreuil‐Monet G, Yao YT, Alderson A, Withers PJ. In situ 3D X‐ray microtomography study comparing auxetic and non‐auxetic polymeric foams under tension. physica status solidi (b). 2011;248:45-51.

[26] Huang YJ, Yang ZJ, Ren WY, Liu GH, Zhang CZ. 3D meso-scale fracture modelling and validation of concrete based on in-situ X-ray Computed Tomography images using damage plasticity model. International Journal of Solids and Structures. 2015;67:340-52.

[27] Ren WY, Yang ZJ, Sharma R, Zhang CH, Withers PJ. Two-dimensional X-ray CT image based meso-scale fracture modelling of concrete. Engineering Fracture Mechanics. 2015;133:24-39.

[28] Huang YJ, Yang ZJ, Chen XW, Liu GH. Monte Carlo simulations of meso-scale dynamic compressive behavior of concrete based on X-ray computed tomography images. International Journal of Impact Engineering. 2016;97:102-15.

[29] Zhang X, Yang ZJ, Huang YJ, Wang ZY, Chen XW. Micro CT Image-based Simulations of Concrete under High Strain Rate Impact using a Continuum-Discrete Coupled Model. International Journal of Impact Engineering. 2021;149:103775.

[30] Housing and Construction Department of Hunan Province. Technical specification for reactive powder concrete structures. 2017. In Chinese.

[31] Buades A, Coll B, Morel J. A non-local algorithm for image denoising. 2005 IEEE Computer Society Conference on Computer Vision and Pattern Recognition (CVPR'05)2005. p. 60-5 vol. 2.

[32] Gastal ESL, Oliveira MM. Adaptive manifolds for real-time high-dimensional filtering. ACM Trans Graph. 2012;31:Article 33.

[33] Li VC, Wang Y, Backer S. Effect of inclining angle, bundling, and surface treatment on synthetic fiber pull-out from a cement matrix. 1990.

[34] Bentur A, Diamond S, Mindess S. Cracking processes in steel fiber reinforced cement paste. Cement & Concrete Research. 1985;15:331-42.

[35] Geuzaine C, Remacle JF. Gmsh: A 3‐D finite element mesh generator with built‐in pre‐and post‐

processing facilities. International journal for numerical methods in engineering. 2009;79:1309-31.

[36] Province HaCDoH. Technical specification for reactive powder concrete structures. -2017.

[37] Ma YF. Study on the constitutive relationship of reactive powder concrete(rpc200) under uni-axial compression: Beijing Jiaotong University; 2006.

[38] Guo X, Kang J, Zhu J. Constitutive relationship of ultrahigh performance concrete under uni-axial compression. J Southeast Univ. 2017;47:369-76.

[39] Hordijk DA. Tensile and tensile fatigue behaviour of concrete; experiments, modelling and analyses. Heron. 1992;37.

[40] Zhang H, Huang YJ, Yang ZJ, Xu SL, Chen XW. A discrete-continuum coupled finite element modelling approach for fibre reinforced concrete. Cement and Concrete Research. 2018;106:130-43.

[41] Cunha VM, Barros JA, Sena-Cruz JM. A finite element model with discrete embedded elements for fibre reinforced composites. Computers & structures. 2012;94:22-33.

[42] Lee Y, Kang S-T, Kim J-K. Pullout behavior of inclined steel fiber in an ultra-high strength cementitious matrix. Construction and Building Materials. 2010;24:2030-41.

Highlights

(1) Ex-situ μXCT tests of UHPFRC beams under bending are carried out for the first time
(2) The whole process of 3D crack initiation and evolution is obtained with various micro/meso-scale failure mechanisms captured by the μXCT images;
(3) Internal 3D microstructures including pores and fibres are statistically quantified and are used to build nonlinear mesoscale FE models of high fidelity;
(4) The simulated load-displacement curves, fracture processes and final crack morphologies are found in excellent agreement with the tests; and
(5) The distribution and orientation of fibres and pores are found to significantly affect damage and fracture evolution from both the tests and the simulations.